ELSEVIER

Pressure–composition–temperature hysteresis in C14 Laves phase alloys Part 2. Applications in NiMH batteries

K. Young*, T. Ouchi, W. Mays, B. Reichman, M.A. Fetcenko

Energy Conversion Devices Inc., 2983 Waterview Drive, Rochester Hills, MI 48309, USA

ABSTRACT

This part of our series of papers reports our efforts to predict sealed cell cycle life from lattice constant a/c ratio and/or PCT hysteresis based on correlations established from our previous studies reported in Part 1. In the case of $Ti_{21}Zr_{12.5}V_{14}Ni_{21.5-x}Cr_{10}Mn_{21}Sn_x$ alloys, as x is increased the a/c ratio increases and the PCT hysteresis decreases resulting in extended cycle life for the battery. This is in agreement with the results from Part 1. In the case of $Ti_{18}Zr_{15.5}V_{14}Ni_{24.2-x}Cr_{10}Mn_{18-y}Sn_{0.3}Co_xAl_y$ alloys, the a/c ratio trend was not observed due to existence of more than one C14 phase, but the correlation between PCT hysteresis and cycle life was maintained. In the case of $Ti_{21}Zr_{12.5}V_{10}Ni_{40.2}Cr_{8.5-x}Mn_{5.6-y}Co_{1.5+x+y}Al_{0.4}Sn_{0.3}$ alloys, the cycle life was dominated by the corrosive nature of the alloy affected by the Cr content. As a consequence, predictions from a/c ratio and PCT hysteresis can only be applied to the degree of pulverization in gas phase cycling and not to the sealed cell cycle life.

© 2009 Elsevier B.V. All rights reserved.

1. Introduction

The nickel metal hydride (NiMH) battery is an emerging technology used both in portable electronic devices and vehicle propulsion applications. The Laves phase AB2 alloy is a good candidate for the negative electrode hydrogen storage material in the NiMH battery. The nature of these AB2 alloys is multi-component with a high degree of disorder [1,2]. The interactions among various constituent components improve the electrochemical characteristic through a synergetic effect [3,4]. When compared to another commonly used misch-metal based AB5 material, AB2 alloy shows a shorter cycle life in NiMH batteries [5–13]. One of the failure modes of the alloy is pulverization through cycling, which has prompted many researchers to focus on controlling the degree of pulverization [14–20]. However, the fabrication and cycle life testing of NiMH batteries are costly and time-consuming. Therefore a technique to forecast the pulverization behavior through a simple testing method is highly desirable to researchers when designing and pre-screening alloy candidates.

In Part 1 of the current series of papers, the mechanic stability of C14 Laves phase alloys was found to be strongly tied with the hysteresis of pressure–concentration–temperature (PCT) isotherms [21]. A larger lattice constant ratio a/c produces a smaller hysteresis between absorption and desorption curves resulting in less stress between α and β phases in the hydride and less pulveriza-tion occurring during charge/discharge cycling. Liu et al. reported the same correlation between pulverization rate and the PCT hysteresis for over-stoichiometric C15 Laves phase alloy [22]. C15 is a face-centered-cubic structure; therefore no correlation can be established between the shape of the unit cell and the PCT hysteresis. Li et al. also reported that pulverization resistance improved with a decrease in PCT hysteresis and an increased a/c ratio in Zr–Mn–Fe alloys [16]. PCT hysteresis was demonstrated to be closely related to the pulverization rate during gas phase cycling of AB5 alloy [23]. In that case, a smaller lattice constant ratio a/c in AB5 alloys corresponded to a smaller hysteresis. Considering the interactions of alloy with hydrogen may be quite different with or without the presence of voltage and electrolyte, Feng et al. used the equilibrium potential to obtain an electrochemical version of PCT isotherm, which is closer to the real hydride/dehydride process happened in a sealed NiMH cell [24].

For this paper, we measured lattice constant, PCT hysteresis, and battery cycle life for three independent alloy systems. The correlation among these measured properties will be analyzed in hopes of developing a pre-screening technique to predict the cycle performance of NiMH batteries.

2. Experimental setup

Induction melting was performed under an argon atmosphere in a 2 kg induction melting furnace using a $MgAl_2O_4$ crucible, an alumina tundish, and a steel pancake-shape mold. A Philips *X'Pert Pro* X-ray diffractometer (XRD) was used to study the micro-structure, and a JOEL-*JSM6320F* scanning electron microscope (SEM) with X-ray energy dispersive spectroscopy (EDS) capability was used to study the phase distribution and composition. A Horiba La-300 Laser Scattering Particle Size Analyzer was used to measure the particle size distribution. PCT characteristics for each

* Corresponding author. Tel.: +1 248 293 7000; fax: +1 248 299 4520.
E-mail address: kwoyoung@yahoo.com (K. Young).

sample were measured using a Suzuki–Shokan multi-channel PCT system. In the PCT analysis, each sample was first activated by a 2-h thermal cycle between 300 °C and room temperature at 25 atm H_2 pressure. PCT isotherm absorption–desorption hysteresis was calculated as the difference in ln(absorption equilibrium pressure at 0.5 wt.% storage) and ln(desorption equilibrium pressure at 0.5 wt.% storage).

For preparation of the sealed battery cells, the ingot was first ground and then sieved below 75 μm. The resulting powder was continuously fed into a roll-compaction mill through a screw feeder together with expanded Ni substrate to form a continuous spool of negative electrode without using any binding material (for a detailed description, see [25]). The typical thickness of the electrode ranged from 0.27 to 0.33 mm. Half cell measurements were conducted using 3.8 cm × 14.0 cm test electrodes cut-out of the continuous belt. The test electrode was initially activated in a 30% KOH bath at 110 °C for 4.5 h. The activated electrode was discharged with a current of 0.05 A (close to 5 mA/g) and then was cycled through charge/discharge cycles with a charge current of 50 mA/g, a discharge current of 50 mA/g and a low rate discharge of 5 mA/g. The cut-off voltage that determined the end of discharge was set at −0.7 V with respect to two pre-activated sintered $Ni(OH)_2$ counter electrodes sandwiching the test electrode.

C-size NiMH batteries were made with metal hydride electrodes cut from the dry compacted continuous belt, combined with pasted $Ni(OH)_2$ counter electrodes (powder A in [26]), 6 M KOH electrolyte, and grafted PP/PE separators. The N/P capacity ratio design was 1.4 to maintain a good balance between the over-charge reservoir and the over-discharge reservoir. The cycle life of each battery was tested by repeating a charge/discharge scheme performed at room temperature. Charging was performed at a C/2 rate with a −ΔV termination method. In the −ΔV termination method, the charging process is terminated when a 3 mV decrease from the maximum cell voltage is detected, indicating the completion of charge and start of hydrogen–oxygen recombination. Discharge was performed at a C/2 rate with a cut-off voltage set at 0.9 V.

3. Results and discussion

3.1. Partial replacement of Ni with Sn

Four alloys substituting Sn for Ni (0, 0.1, 0.2, and 0.4 at.%) in the base alloy $Ti_{21}Zr_{12.5}V_{14}Ni_{21.5}Cr_{10}Mn_{21}$ were made by induction melting (alloys #1–#4 in Table 1). Both structural and electrochemical properties were previously reported [27]. Results from XRD analysis indicated the alloys are all dominated by the C14 crystal structure and calculated lattice constants are listed in Table 1. As the amount of Sn-substitution increased, the lattice constant ratio a/c decreased. PCT isotherms measured at 30 °C are plotted in Fig. 1 and the hysteresis for these four alloys measured at 0.5 wt.% capacity is listed in Table 1. As Sn amount increased, the PCT hysteresis increased, which follows the trend of lattice constant ratio as predicted in Part 1 [21].

These four alloys were made into NiMH batteries and their cycle life was previously reported [27]. In Fig. 2, both PCT hysteresis measured at 30 °C and 60 °C were plotted against the end-of-life cycle, which is defined as the first cycle the cell capacity drops below 70% of its initial value. It is clear from this figure that alloys with lower PCT hysteresis cycle are better than alloys with higher hysteresis. Therefore, we conclude that a/c ratio, PCT hysteresis, and cycle life performance are all in good agreement in the case of partial replacement of Ni with Sn.

3.2. Changing Ni/Co/Al contents

Four alloys were made by induction melting to study the effect of adding Co contents in the alloy formula (alloys #5–#8 in Table 1). The base alloy, $Ti_{18}Zr_{15.5}V_{14}Ni_{24.2}Cr_{10}Mn_{18}Sn_{0.3}$, is a modification of alloy #1 with a higher Zr/Ti ratio to increase the capacity of the alloy [28]. Additionally, 0.5 at.% of Al was added to #6, #7, and #8 to improve the high-rate discharge performance.

The C14 Laves phase dominated the XRD spectra for alloys #5–#8 as shown in Fig. 3. There are two C14 phases observed in alloys #5, #6, and #8 (multi-component features peak around 73°). The calculated a, c, and a/c values are listed in Table 1. Due to the existence of more than one C14 phase, a clear trend of a/c ratio similar to the previous case cannot be established. PCT isotherms obtained from 30 °C measurement for alloys #5–#8 are plotted in

Table 1
Composition, structure parameters, PCT hysteresis and cycle life of alloys in this study.

Alloy number	Alloy formula	Crystal structure	Lattice constant, a (in Å)	Lattice constant, c (in Å)	Lattice constant ratio (a/c)	30 °C PCT hysteresis $\ln(P_a/P_d)$	Cycle reaching 70% capacity
1	$Ti_{21}Zr_{12.5}V_{14}Ni_{21.5}Cr_{10}Mn_{21}$	100% C14	4.941	8.068	0.6124	0.14	121
2	$Ti_{21}Zr_{12.5}V_{14}Ni_{21.4}Cr_{10}Mn_{21}Sn_{0.1}$	100% C14	4.933	8.058	0.6122	0.26	104
3	$Ti_{21}Zr_{12.5}V_{14}Ni_{21.3}Cr_{10}Mn_{21}Sn_{0.2}$	100% C14	4.945	8.081	0.6119	0.32	74
4	$Ti_{21}Zr_{12.5}V_{14}Ni_{21.1}Cr_{10}Mn_{21}Sn_{0.4}$	100% C14	4.947	8.087	0.6117	0.48	68
5	$Ti_{18}Zr_{15.5}V_{14}Ni_{24.2}Cr_{10}Mn_{18.0}Sn_{0.3}$	100% C14	4.987, 4.957	8.144, 8.107	0.6123, 0.6114	0.51	120
6	$Ti_{18}Zr_{15.5}V_{14}Ni_{23.7}Cr_{10}Mn_{17.5}Sn_{0.3}Co_{0.5}Al_{0.5}$	100% C14	4.996, 4.963	8.159, 8.093	0.6124, 0.6133	0.24	125
7	$Ti_{18}Zr_{15.5}V_{14}Ni_{22.7}Cr_{10}Mn_{17.5}Sn_{0.3}Co_{1.5}Al_{0.5}$	100% C14	4.969	8.123	0.6117	0.17	145
8	$Ti_{18}Zr_{15.5}V_{14}Ni_{21.7}Cr_{10}Mn_{17.5}Sn_{0.3}Co_{2.5}Al_{0.5}$	100% C14	4.984, 4.959	8.180, 8.124	0.6092, 0.6104	0.13	165
9	$Ti_{12.5}Zr_{21}V_{10}Ni_{40.2}Cr_{8.5}Mn_{5.6}Co_{1.5}Al_{0.4}Sn_{0.3}$	87% C14, 13% C15	4.966	8.111	0.6123	0.13	955
10	$Ti_{12.5}Zr_{21}V_{10}Ni_{40.2}Cr_{5.5}Mn_{5.1}Co_{5.0}Al_{0.4}Sn_{0.3}$	53% C14, 47% C15	4.964	8.102	0.6127	0.06	790
11	$Ti_{12.5}Zr_{21}V_{10}Ni_{40.2}Cr_{3.5}Mn_{4.1}Co_{8.0}Al_{0.4}Sn_{0.3}$	28% C14, 72% C15	4.967	8.094	0.6137	0.02	510
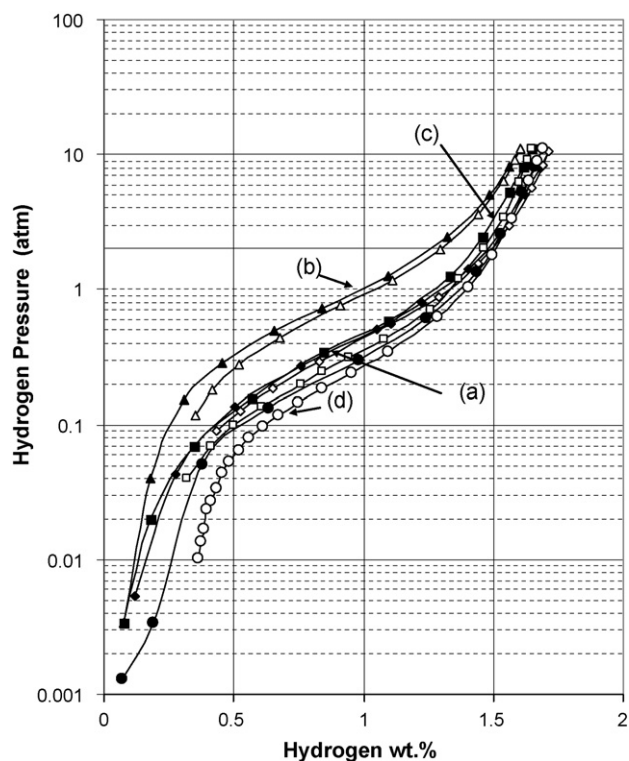
Fig. 1. PCT absorption and desorption isotherms measured at 30 °C for alloys #1 (a, ♦), #2 (b, ▲), #3 (c, ■), and #4 (d, ●), where solid symbols are for absorption isotherms while open symbols are for desorption isotherms.

Fig. 3. XRD spectra using Cu Kα as the radiation source for alloys #5 (a), #6 (b), #7 (c), and #8 (d).

3.3. Increase of Co at the cost of Mn and Cr

In the previous two examples, all of the alloys have a predominantly C14 crystal structure and a correlation between PCT and cycle life was demonstrated. Below we report some work on mixed C14/C15 phase alloys where the correlation between larger a/c and smaller PCT hysteresis is still valid but the final cycle life was affected by other factors, such as the co-existence of another major hydrogen storage phase and/or alloy corrosion.

Three alloys were made by induction melting with different Cr/Mn/Co contents and their compositions are listed as alloys #9, #10, and #11 in Table 1. The average atomic radii for A atoms and B atoms were calculated based on the atomic radii of constituent ele-

Fig. 4. The small amount of additional Co and Al do not change the maximum hydrogen storage capacity or the plateau pressure. However, a substantial reduction in PCT hysteresis can be seen from calculated values listed in Table 1.

Alloys #5–#8 were made into C-size NiMH batteries and the cycle life testing results are plotted in Fig. 5. As more Co was added into the formula at the expense of Ni, the cycle life was extended, as predicted from the smaller PCT hysteresis. Therefore, the conclusion of this section is that for a multi-component system, the a/c ratio is not a good indicator in predicting cycle performance but PCT hysteresis still correlates very well with the cycle life in the sealed cell.
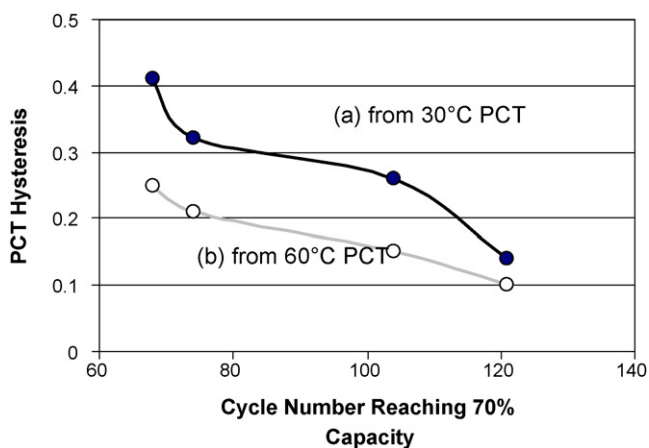

Fig. 2. Plot of 30 °C and 60 °C PCT hysteresis at 0.5% storage vs. cycle number when capacity dropped below 70% of its original capacity.
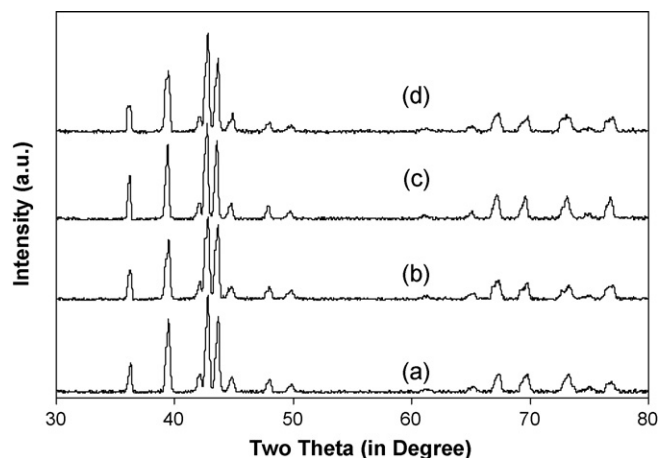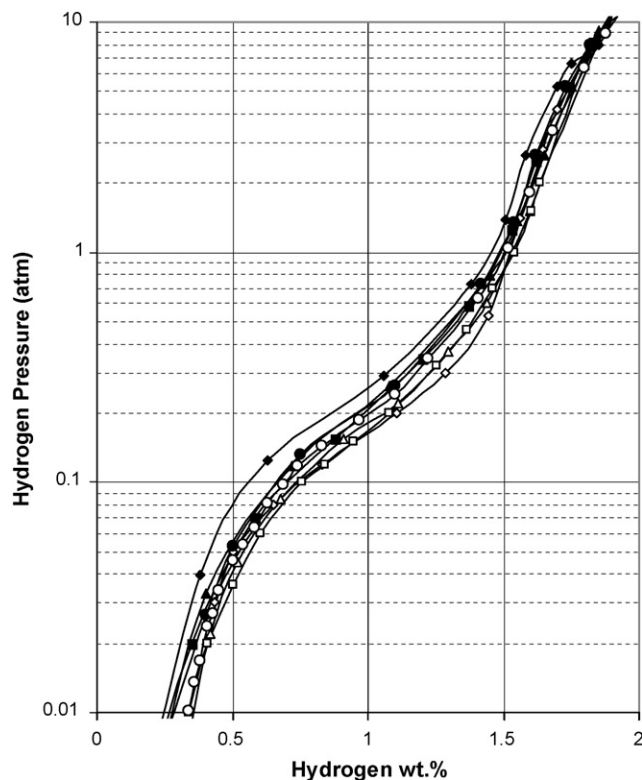

Fig. 4. PCT absorption and desorption isotherms measured at 30 °C for alloys #5 (♦), #6 (▲), #7 (■), and #8 (●), where solid symbols are for absorption isotherms while open symbols are for desorption isotherms.
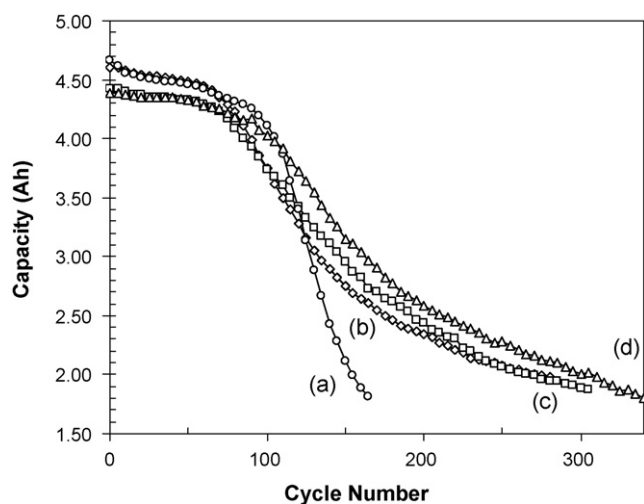
Fig. 5. Cycle life of sealed NiMH batteries measured by a C/2 charge rate with a $-\Delta V$ of 3 mV termination and a C/2 discharge rate with a cut-off voltage of 0.9 V for alloys #5 (a, ○), #6 (b, ◇), #7 (c, □), and # 8 (d, △).

ments listed in ref. [29]. The r_A/r_B ratio increases from 1.217 for alloy #9 to 1.218 for alloy #10 and then to 1.219 for alloy #11. The ratios are approaching but still lower than the C14/C15 threshold at 1.225 and a predominantly C14 crystal structure is expected based on work done with Zr-based Laves phase alloys [30]. XRD analysis was performed and the resulting spectra are plotted in Fig. 6. All reflections from C15 structure align very well with some of those from C14 structure. The Rietveld analysis of alloys #9, #10, and #11 indicated that the percentage of C15 phase in the alloys are 13%, 47%, and 72%, respectively. The C15 percentages increase as the alloys r_A/r_B ratios increase. The general trend of lattice structure is consistent with the prediction from atomic radii with a lower C14/C15 threshold (1.218–1.219 in stead of 1.225). The real atomic radius of the element will deviate from the metallic radius according to the difference in electronegativity between neighboring atoms [31] and therefore a shift in the C14/C15 threshold is acceptable. Furthermore, the C14/C15 mixtures in alloys #10 and #11 do not conform to the criterion functions for forming the C15 phase as predicted from valance charge density using equation 12 from ref. [32] and from average electron concentration [33]. The multi-element, multi-phase alloys are too complicated to be handled by models built from simple binary alloys.
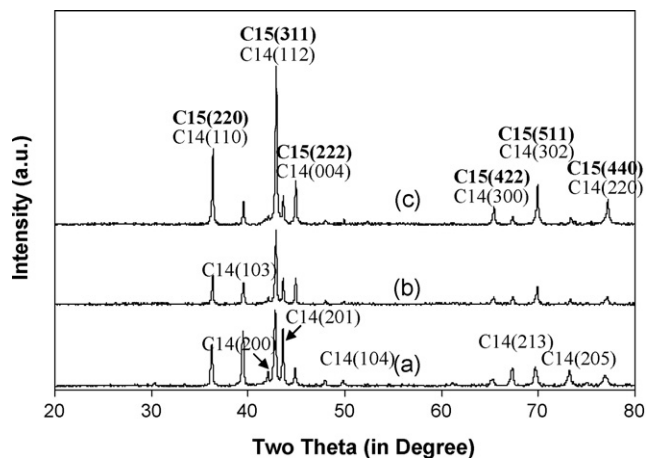
Fig. 6. XRD spectra using Cu Kα as the radiation source for alloys #9 (a), #10 (b), and #11 (c). Miller indices from C15 reflection are in bold to distinguish them from C14 reflections.
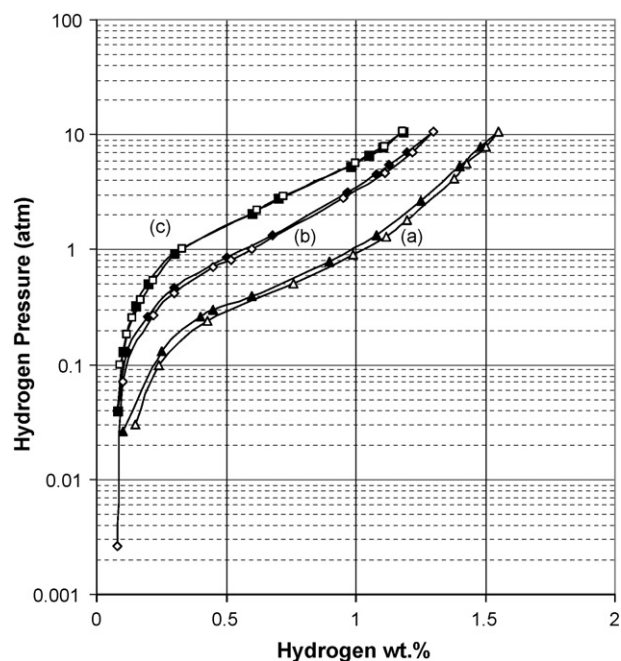
Fig. 7. PCT absorption and desorption isotherms measured at 30 °C for alloys #9 (a, ▲), #10 (b, ♦), and #11 (c, ■), where solid symbols are for absorption isotherms while open symbols are for desorption isotherms.

Lattice constants a and c from the C14 phase, and the calculated a/c ratio are listed in Table 1. Lattice constant a remains roughly the same while lattice constant c decreases as the amount of Co is increased. The shrinkage of cell volume comes from the relatively smaller size of Co when compared to Cr and Mn. The a/c ratio increases with higher Co which should contribute to a reduction in PCT hysteresis according to the discussion in the Part 1 of these two consecutive papers [21].

PCT isotherms were taken at 30 °C for all three alloys and are plotted in Fig. 7. The plateau pressure increases with the amount of Co, which is the consequence of both a smaller lattice volume and a higher valence electron density. As expected there was a reduction in PCT hysteresis with a higher Co content, which complies with the prediction from a higher a/c ratio.

C-sized cells were made from alloys #9 to #11. The cycle life testing results are plotted in Fig. 8. The cycle life of cells made from alloy #9 was greater than that of cells made from alloy #10, which in turn was greater than the cycle life of cells made from alloy #11. This electrochemical cycling result is different that what is predicted by the a/c ratio and PCT hysteresis. In order to study the discrepancy, we performed a gas phase cycling experiment. After 50 hydride/dehydride cycles, the particle size distribution of each alloy was measured and is plotted in Fig. 9. Alloy #9 with the smallest a/c ratio and largest PCT hysteresis is the one which was pulverized the most (curve a in Fig. 9). Therefore the electrochemical cycle life shown in Fig. 8 was not dictated by the pulverization rate.

In order to eliminate the possibility of C14/C15 phase mixture causing the short cycle life, SEM analysis was performed on alloys #9–#11 with the back scattering image micrographs shown in Fig. 10. EDS results from selected areas on each micrograph identified by numbers are listed in Table 2. The brightest spots are from Zr metal and the darkest areas are from ZrO_2. The main phases are all AB2-stoichiometric with very small variations in chemical composition. The AB2 phase size and proximity in all three alloys are similar. Besides the main AB2 phase, TiNi (a1, b5, and c5) and Zr_9Ni_{11} (b2) secondary phases are found. Since the multi-component features in alloys #9–#11 are similar, we came to the conclusion that phase segregation was not the main factor driving cycle life perfor-
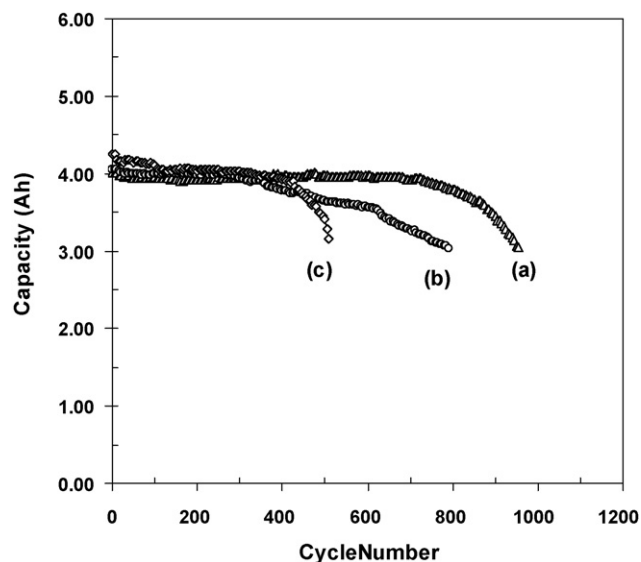
Fig. 8. Cycle life of sealed NiMH batteries measured by a $C/2$ charge rate with a $-\Delta V$ of 3 mV termination and a C/2 discharge rate with a cut-off voltage of 0.9 V for alloys #9 (a), #10 (b), and #11 (c).
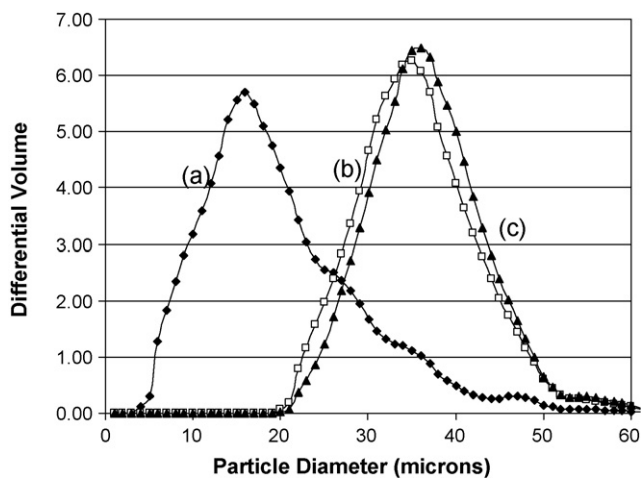

Fig. 9. Particle size distribution curves for alloys #9 (a, ◆), #10 (b, □), and #11 (c, ▲) after 50 gas phase hydride/dehydride cyclings.

Table 2
EDS results measured from spots identified in micrographs shown in Fig. 10. All numbers listed here are in atomic percents.

|	Zr	Ti	V	Ni	Cr	Mn	Co	Al
a1	19.8	21.8	1.6	52.8	0.9	1.8	0.7	0.6
a2	22.2	10.3	9.9	42.3	7.6	5.6	1.1	0.8
a3	22.0	10.0	10.2	43.1	7.2	5.5	1.3	0.9
a4	22.1	11.5	8.8	44.9	5.9	5.0	1.1	0.7
a5	100.0	0.0	0.0	0.0	0.0	0.0	0.0	0.0
b1	34.7	13.0	6.8	34.3	3.1	3.5	3.6	0.9
b2	20.9	13.0	9.7	39.9	5.1	5.1	4.9	1.3
b3	21.3	11.6	11.1	38.4	5.6	5.5	5.1	1.5
b4	21.0	13.1	8.4	42.2	4.4	4.6	4.6	1.7
b5	17.7	25.5	1.7	47.6	0.9	1.8	3.6	1.2
b6	100.0	0.0	0.0	0.0	0.0	0.0	0.0	0.0
c1	100.0	0.0	0.0	0.0	0.0	0.0	0.0	0.0
c2	22.2	10.1	12.1	35.4	4.7	5.2	9.0	1.3
c3	21.3	10.8	10.7	39.3	4.0	4.6	8.3	1.1
c4	21.4	11.4	10.5	38.8	3.7	4.7	8.4	1.2
c5	16.5	26.9	1.8	45.8	0.5	1.7	5.9	1.1
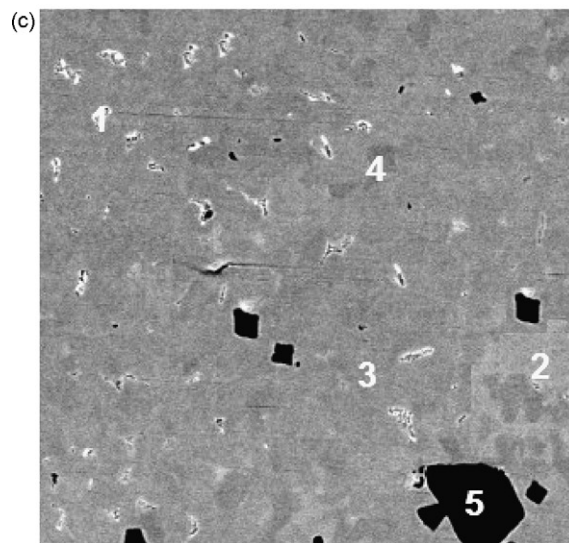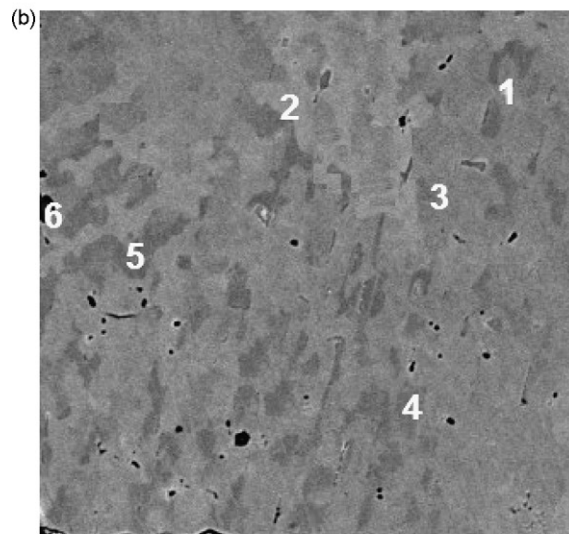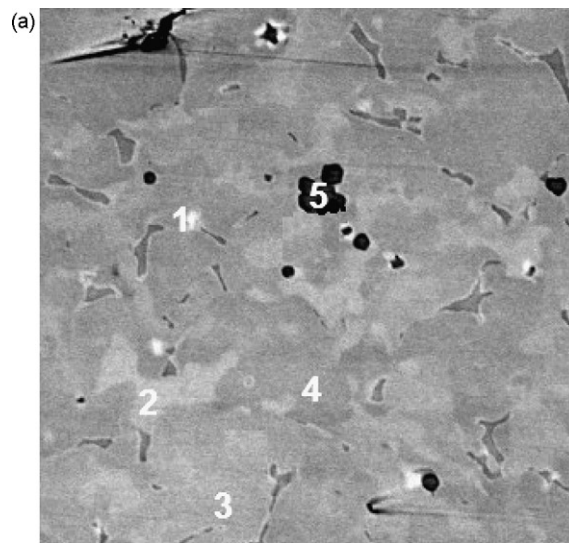
Fig. 10. SEM backscattering electron image micrographs for alloys (a) #9, (b) #10, and (c) #11. Numbers in each micrograph indicate EDS analyses were done in these areas and chemical compositions are summarized in Table 2.

mance. Further XRD studies from the partially hydrided alloys #10 and #11 indicated that both C14 and C15 phase absorbed hydrogen at the same time and no wedge effect was found between these two phases.

The only remaining untouched difference among alloys #9–#11 is the chemical composition. The enhancement of cycle durability in Ti–Zr–V–Mn–Ni alloy by adding the proper amounts of Cr, mainly due to its contribution to the corrosion resistance, have been reported [14,34–36]. We have performed corrosion studies on these three alloys by preparing a polished ingot surface and measuring the polarization resistance (R_p) using the linear polarization method with a voltage swing of 20 mV about the open-circuit voltage with respect to a Hg/HgO reference electrode. The corrosion current was then calculated using the Stern–Geary relationship:

$$I_{corr}(A/cm^2) = \frac{B_a B_c}{2.3(B_a + B_c)R_p}$$

where B_a and B_c are the anodic and cathodic tafel slopes, respectively. Since the tafel slopes could not be calculated from this data, 0.12 V/decade are often used resulting in the Stern–Geary coefficients (SGC) [37]:

$$SGC = \frac{B_a B_c}{2.3(B_a + B_c)} = 0.026$$

$$I_{corr}(A/cm^2) = \frac{0.026}{R_p}$$

The obtained corrosion current densities are 43, 56, and 60 μA/cm^2 for alloys #9–#11, respectively. It is apparent from the data that with decreasing amounts of Cr the corrosion current density increased, therefore more metal corrodes resulting in a degraded cycle life.

The cycle life is always a difficult problem to solve and can be affected by many factors. Pulverization due to stress from hydride/metal interface is one factor causing degradation of cycle life. Pulverization can be predicted from a/c ratio and/or PCT hysteresis. After eliminating pulverization issues, other factors, such as surface corrosion, oxide passivation, phase segregation, dissolution and poisoning positive electrode, etc. start to play an important role in cycle life performance.

4. Conclusions

In this second of two consecutive papers on the PCT hysteresis of Laves phase alloys, three examples are presented to validate the correlation developed in Part 1 using simple ternary alloys. In the case of changing Ni/Sn content in C14-predominated alloys, a higher a/c ratio results in a smaller PCT hysteresis, and also an improvement in the electrochemical cycle stability. In the case of multi-C14 present in the alloy, only the correlation between PCT hysteresis and cycle life can be established. In the case of C14/C15 mixed alloys, a higher

a/c ratio leads to a smaller PCT hysteresis and less pulverization in the gas phase cycling test. However, the electrochemical cycle life tests were greatly affected by the corrosive nature of the alloys. Although alloy #11 has the largest a/c ratio, its cycle life was limited by the relatively poorer corrosion resistance due to a reduction in Cr-content. Therefore we conclude that either a/c ratio or PCT hysteresis can be used to predict the degree of pulverization during cycling, but more factors have to be taken into consideration with battery cycle life.

References

[1] S.R. Ovshinsky, M.A. Fetcenko, J. Ross, Science 260 (1993) 176.
[2] Q.A. Zhang, Y.Q. Lei, J. Alloys Compd. 368 (2004) 362.
[3] Q.A. Zhang, Y.Q. Lei, X.G. Yang, K. Ren, Q.D. Wang, J. Alloys Compd. 292 (1999) 236.
[4] K. Young, T. Ouchi, Y. Liu, B. Reichman, W. Mays, M.A. Fetcenko, unpublished.
[5] H.-H. Lee, K.-Y. Lee, J.-Y. Lee, J. Alloys Compd. 253–254 (1997) 601.
[6] J. Chen, S.X. Dou, H.K. Liu, J. Alloys Compd. 256 (1997) 40.
[7] B. Knosp, L. Vallet, Ph. Blanchard, J. Alloys Compd. 293–295 (1999) 770.
[8] S. Lee, H. Lee, J. Kim, P.S. Lee, J. Lee, J. Alloys Compd. 308 (2000) 209.
[9] B.H. Liu, Z.P. Li, R. Kitani, S. Suda, J. Alloys Compd. 330–332 (2002) 825.
[10] K. Yang, D. Chen, L. Chen, Z. Guo, J. Alloys Compd. 333 (2002) 184.
[11] Y. Xu, C. Chen, X. Wang, Y. Lei, Q. Wang, J. Alloys Compd. 337 (2002) 214.
[12] Y. Zhu, H. Pan, M. Gao, J. Ma, Y. Lei, Q. Wang, Int. J. Hydrogen Energy 28 (2003) 311.
[13] Y. Xu, C. Chen, X. Wang, Y. Lei, X. Wang, L. Chen, Q. Wang, Int. J. Hydrogen Energy 32 (2007) 1716.
[14] S. Kim, K. Lee, J. Lee, J. Alloys Compd. 223 (1995) 22.
[15] T. Bratanich, S. Solonin, V. Petrischev, V. Skorokhod, Int. J. Hydrogen Energy 21 (1996) 1115.
[16] M. Wada, H. Uchida, H. Kaneko, J. Alloys Compd. 258 (1997) 42.
[17] X.-P. Gao, Y.-M. Sun, E. Toyoda, E. Higuchi, T. Nakagima, S. Suda, J. Power Sources 83 (1990) 100.
[18] X.-P. Gao, Y.-M. Sun, E. Toyoda, E. Higuchi, T. Nakagima, S. Suda, Electrochim. Acta 45 (2000) 3099.
[19] X.Z. Sun, Y.F. Zhu, Y. Lin, R. Li, M.X. Gao, H.G. Pan, Acta Metall. Sin. (Engl. Lett.) 19 (2006) 68.
[20] S.L. Li, H.H. Cheng, X.X. Deng, W. Chen, D.M. Chen, K. Yang, J. Alloys Compd. 460 (2008) 186.
[21] K. Young, T. Ouchi, M.A. Fetcenko, J. Alloys Compd 480 (2009) 428.
[22] B.H. Liu, Z.P. Li, S. Suda, J. Electrochem. Soc. 149 (2002) A537.
[23] Y. Osumi, Suiso-kyuzo-goukin no Syurui to Sono, new ed., Agune Technology Center, Tokyo, Japan, 1999, p. 218.
[24] F. Feng, X. Ping, Z. Zhou, M. Geng, J. Han, D.O. Northwood, Int. J. Hydrogen Energy 23 (1998) 599.
[25] D. Magnuson, M. Wolff, S. Lev, K. Jeffries, S.D. Mapes, US Patent 4,670,214 (1987).
[26] C. Fierro, A. Zallen, J. Koch, M.A. Fetcenko, J. Electrochem. Soc. 153 (2006) A492.
[27] K. Young, M.A. Fetcenko, T. Ouchi, F. Li, J. Koch, J. Alloys Compd. 469 (2009) 406.
[28] K. Young, M.A. Fetcenko, F. Li, T. Ouchi, J. Alloys Compd. 464 (2008) 238.
[29] Nihon Kinzoku Gakkai, Hi Kagaku Ryouronteki Kinzoku Kagobutu, Maruzen, Tokyo, 1975, p. 296.
[30] H. Nakano, I. Wada, S. Wakao, J. Adv. Sci. 4 (1992) 239.
[31] F. Stein, M. Palm, G. Sauthoff, Intermetallics 12 (2004) 713.
[32] W. Jiang, C. Huang, D. Huang, X. Jian, J. Guo, Acta Metallurgica Sinica 41 (2005) 19.
[33] Z.H. Zhu, C.T. Liu, P.K. Liaw, Intermetallics 7 (1999) 1011.
[34] J. Yu, S. Lee, K. Cho, J. Lee, J. Electrochem. Soc. 147 (2000) 2013.
[35] G.Y. Wang, Y.H. Xu, H.G. Pan, Q.D. Wang, Int. J. Hydrogen Energy 28 (2003) 499.
[36] H. Pan, R. Li, M. Gao, Y. Liu, Q. Wang, J. Alloys Compd. 404–406 (2005) 669.
[37] F. Mansfeld, in: M.G. Fontana, R.W. Staehle (Eds.), Advances in Corrosion Science and Technology, 6th ed., Plenum Press, 1976, p. 163.